Omnidirectional Visual Odometry for Flying Robots using Low-power Hardware

Simon Reich, Maurice Seer, Lars Berscheid, Florentin Wörgötter and Jan-Matthias Braun
Third Institute of Physics - Biophysics, Georg-August-Universität Göttingen, Friedrich-Hund-Platz 1, 37077 Göttingen, Germany

Keywords: Visual Odometry, Embedded Hardware, Omnidirectional Vision.

Abstract: Currently, flying robotic systems are in development for package delivery, aerial exploration in catastrophe areas, or maintenance tasks. While many flying robots are used in connection with powerful, stationary computing systems, the challenge in autonomous devices—especially in indoor-rescue or rural missions—lies in the need to do all processing internally on low power hardware. Furthermore, the device cannot rely on a well ordered or marked surrounding. These requirements make computer vision an important and challenging task for such systems. To cope with the cumulative problems of low frame rates in combination with high movement rates of the aerial device, a hyperbolic mirror is mounted on top of a quadrocopter, recording omnidirectional images, which can capture features during fast pose changes. The viability of this approach will be demonstrated by analysing several scenes. Here, we present a novel autonomous robot, which performs all computations online on low power embedded hardware and is therefore a truly autonomous robot. Furthermore, we introduce several novel algorithms, which have a low computational complexity and therefore enable us to refrain from external resources.

1 INTRODUCTION

Real time computer vision in fast moving robots remains still a very challenging task, especially when forced to use limited computing power, e.g. when having to use embedded systems. There are several robotic applications existing where this is needed and one of the most challenging is visual guided on-board-computed indoor flight. There are no GPS signals available and the autonomous aerial vehicle (AAV) has to navigate quickly in often confined spaces. To enable collision detection, onboard sensors must be utilized. The probably most prominent autonomous robot is the unmanned car Stanley, which won the DARPA Grand Challenge in 2005 (Thrun et al., 2006). Stanley has a wide range of different sensors, including GPS, laser range sensors, and RADAR sensors: The total power consumption accumulates to 500 W (Thrun et al., 2006).

In recent years, energy efficient hardware, which is still powerful enough, and batteries, which offer enough power, became available. This allowed on the one hand for smaller robots and on the other hand for complex motor control tasks and sensor evaluation—as it is required in quadrocopters. However, active sensors approaches often lack in high power requirements and heavy weight. Both problems are solved by using an RGB camera, which is a passive sensor and has low power consumption.

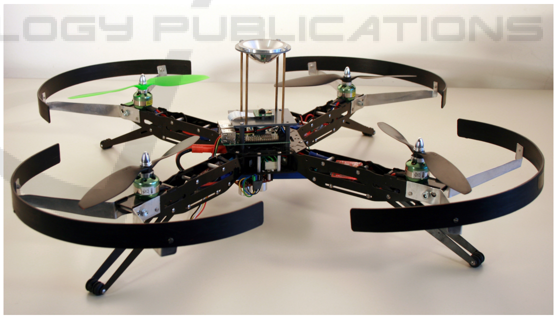
Figure 1: The quadrocopter utilized in this work. In the center, a camera captures omnidirectional images via the mounted mirror (Compare Fig. 3a).

Previous work on autonomous flight can be categorized into two research areas. First, a lot of works focus on agile and accurate motion control. Most prominent is the quadrocopter swarm of ETH Zurich, which is able to perform synchronized dancing motions (Schöllig et al., 2012) or even to build simple architectural structures (Augugliaro et al., 2014). But these complex tasks heavily rely on external tracking of the robots and are thus restricted to lab use. In another approach, artificial markers in the environment simplify pose estimation (Eberli et al., 2011). For GPS enabled areas, complete commercial solutions exist, e.g. (Remes et al., 2013; Anai et al., 2012).

Second, there are approaches, which only use online sensors for self localization. Still, in many studies the computational expensive tasks are performed on external hardware via Bluetooth or wireless LAN links, e.g. (Engel et al., 2014; Teuliére et al., 2010), which limit the independence of the devices. In recent years, the miniaturization of computers and advancement in battery design, driven mostly by rapid cell phone development, has made it possible to build smaller autonomous robots and perform computations in real time on the AAV itself. While online computations result in maximum autonomy, even today, real time computations on 3D data remain a complex task. Instead of 3D sensors as LIDAR, the Asus Xtion Pro, or the Microsoft Kinect sensor, most systems use a monocular camera and perform 3D reconstruction.

For example, already in 2010 in (Olivares-Méndez et al., 2010) detection of a planar landing zone for a helicopter using a monocular camera is described, allowing for autonomous landing of a helicopter. (Mori and Scherer, 2013) use a front facing camera to detect objects in the flight path and estimate size. Yet, all approaches with camera in a specific direction face the problem of a small observation window.

Omnidirectional monocular cameras, which provide a 360° view of the environment, have been successfully applied to these problems. In (Gaspar et al., 2001), a slow moving robot estimates the depth of edges in a corridor using an omnidirectional camera. (Rodríguez-Canosa et al., 2012) apply this procedure to an unstable flying robot; however, no quantitative results are shown. In (Demonceaux et al., 2006) this method is shown to be able to achieve attitude measurements.

In this work, we focus on navigating a flying robot in unknown, GPS-denied, indoor scenarios. All computations are performed online and in real time—there will be no external tracking. We ask: what is needed to safely (and therefore reliably) detect features on a hardware platform that very strongly jerks, jolts, and may even flip? And—if those can be found—how to track them and use them for trajectory planning on limited hardware in real time? One goal is to improve navigation by introducing a novel lightweight omnidirectional camera setup for embedded computer systems. Lastly, we aim to extract features, track them over multiple frames, compute a 3D point cloud, and perform high level navigation tasks on this internal model of the AAV's environment.

In the following section, we shortly introduce our hardware approach, a quadrocopter holding an omnidirectional camera. Afterwards, the utilized algorithms are shown. Then, we describe our experiments and results, followed by a detailed discussion and conclusion.

2 METHOD

This section divides into three parts: In 2.1 the hardware setup is presented, and in 2.2 our algorithms to arrive at safe trajectory planning are shown. Lastly, we will discuss briefly the theoretical limit of the algorithms.

2.1 Hardware Setup

The hardware setup is depicted in Fig. 1: A quadrocopter, controlled by a Raspberry Pi mini computer. These robots are able to turn and even flip on very short notice. This poses the problem that a front facing camera is not able to reliably track features, as it has to deal with huge offsets and many features leaving the camera's field of view. We therefore attached a monocular camera pointing upwards on a hyperbolically shaped mirror, which can also be replaced with a spherical shaped mirror. Later, we will discuss the advantages and disadvantages of these shapes. The camera photographs with a resolution of 320x320 px at a frequency of 30 Hz.

Additionally, we use an accelerometer and gyroscope as input. Also, any contemporary Bluetooth gaming controller can be attached. This allows easy control of high level features, e.g. issue the start or landing command. The 6D pose from the visual odometry algorithm is merged with data from an accelerometer and a gyroscope using a Kalman filter. All software components run as modular and parallel nodes using the Robot Operating System (ROS (Quigley et al., 2009)).

2.2 Algorithms

In this section, we describe how we estimate the AAV's pose from an omnidirectional monocular RGB images. All software components run as parallel nodes using the Robot Operating System (ROS (Quigley et al., 2009)).

An overview of the proposed system is given in Fig. 2. First, we compute features and the optical flow based on the raw camera image. Dewarping the image enables us to estimate the pose change from the last

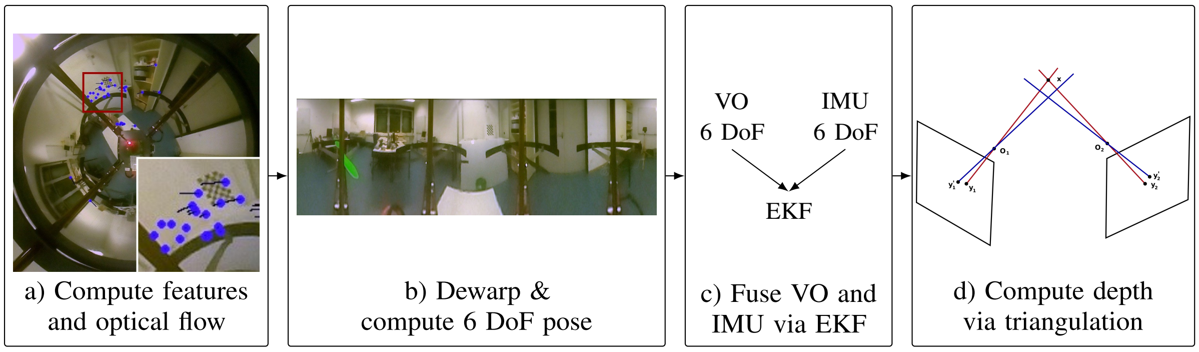
a) Compute features and optical flow
b) Dewarp & compute 6 DoF pose
VO 6 DoF
IMU 6 DoF
EKF
c) Fuse VO and IMU via EKF
d) Compute depth via triangulation

Figure 2: Pipeline of our proposed algorithm. a) Based on features we compute the optical flow. b) After dewarping the image, we estimate the pose change. c) An Extended Kalman Filter (EKF) combines the Visual Odometry (VO) results with values from the Inertial Measurement Unit (IMU). d) After having tracked features for multiple frames, we can estimate the point's depth using triangulation and build a depth map.

camera frame (Fig. 2b). An Extended Kalman Filter (EKF) (Kalman, 1960) fuses the visual odometry 6 DoF results with the 6 DoF of the Inertial Measurement Unit (Fig. 2c). Afterwards, a PID controller, as demonstrated by (Åström and Hägglund, 2006), adjusts the motor controllers to manipulate the quadrocopter into the goal pose (which is defined by e.g. SLAM (Williams et al., 2009), corridor flight algorithms (Lange et al., 2012), etc.). As we keep a list of all tracked features and their relative position to the robot, we can triangulate each feature and compute a depth estimate for each feature (Fig. 2d). This can be used by high level algorithms for map building or navigation tasks.

2.2.1 Feature Set

As already mentioned, we first compute features on the raw camera image. Features are points in an image, which are easy to find, recognize, and track in consecutive frames—usually areas rich in texture. Afterwards, we compute the optical flow on these features. There are numerous publications comparing different feature algorithms—the most prominent algorithms include FAST (Rosten and Drummond, 2006), GFTT (Shi and Tomasi, 1994), ORB (Rublee et al., 2011), SIFT (Lowe, 1999), and SURF (Bay et al., 2006). Here, we use FAST as it offers a good FAST offers the best trade-off between computational complexity and quality of found features. This result is not surprising, as FAST is known to be faster but also finds less features (El-gayar et al., 2013; Heinly et al., 2012).

2.2.2 Transformations between Image and World Coordinates

In the following, we derive transformations $T_{S,H}$ from image space to the external frame of reference and

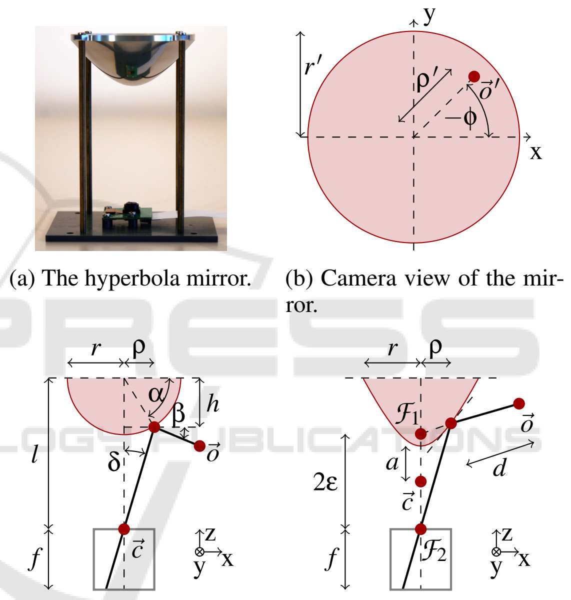

(a) The hyperbola mirror. (b) Camera view of the mirror. (c) Side view of spherical mirror. (d) Side view of hyperbola mirror.

Figure 3: Sketch of a camera observing an object $\vec{o}$, which appears at position $\vec{o}'$ in the image plane (bottom left). The top left figure depicts a simple pinhole model; on the top right the camera is pointed at a spherical mirror and at the bottom right at a hyperbolic mirror.

their inverse $T_{S,H}^{-1}$. T_S indicates a spherical and T_H a hyperbola shaped mirror. We denote object positions in image space by 2D coordinates $\vec{o}'$ in cartesian (o'_x, o'_y) or polar coordinates (ρ, ϕ). We denote their counterparts in the external frame of reference as $\vec{o} \in \mathbb{R}^3$. The robot's pose in the external frame of reference is determined by its position $\vec{c}$ and orientation $\vec{q}$: This is the pose of the camera's view as shown in Fig. 3c and 3d. As the derivation of the transformation includes several coordinate system changes, we here present the transformations.

Spherical Mirror Model. A spherical mirror is mounted with its center in distance l above the camera (Fig. 3c). Using the real sphere radius r and radius r' in image space (Fig. 3b), the reflection's position on the mirror can be computed independently of camera parameters using the scaling factor $s = {}^{r}/_{r'}$. With the unit vector $\vec{e}$ pointing from the reflection on the mirror towards the object's position $\vec{o}$

$$\vec{e}_S(\vec{o}\,') = \begin{pmatrix} \cos\beta\cos\phi \\ \cos\beta\sin\phi \\ -\sin\beta \end{pmatrix} \quad ,$$

given the distance d, $h = \sqrt{r^2 - \rho^2}$, the angles in Fig. 3b derived from the image coordinates, and the rotation matrix $R(\vec{q})$ between the external frame of reference and the camera system in Fig. 3b, we can compute the position $\vec{o}$ by:

$$T_S : \vec{o}\,' \longmapsto \vec{o} : \vec{o} = \vec{c} + R(\vec{q}) \left(\begin{pmatrix} so'_x \\ so'_y \\ l - h(\vec{o}\,') \end{pmatrix} + d\vec{e}_S(\vec{o}\,') \right).$$

For the inverse transformation T_S^{-1}, we use polar coordinates:

$$T_S^{-1} : \vec{o} \longmapsto \vec{o}\,' : \vec{o}\,' = r' \cos\alpha(\vec{o}) \cdot \begin{pmatrix} \cos\phi(\vec{o}) \\ \sin\phi(\vec{o}) \end{pmatrix} \quad ,$$

with $\phi = -\operatorname{atan2}\left((R^{-1}(\vec{q})(\vec{o}-\vec{c}))_y, (R^{-1}(\vec{q})(\vec{o}-\vec{c}))_y\right)$ and $\rho' = r' \cos\alpha(\vec{o})$. As there is no explicit form for $\cos\alpha$, we use the iterative approximation

$$\cos\alpha \approx \left(\frac{l}{r} - \sin\alpha\right) \cdot \tan\left(\arctan\left(\frac{-\sin\alpha - \Delta\sin\beta}{r\cos\alpha}\right) - 2\alpha + \frac{\pi}{2}\right),$$

for small focal lengths ($l - f \approx l$) and large depths (${}^{d}/_{r} \ll 1$).

Still, the solution is nontrivial and computational expensive. Considering that we are using autonomous robots, which perform all computations online on limited hardware, this poses a problem.

Hyperbolic Mirror Model. Using a hyperbola, the inverse function can be computed easier and thus faster. The surface of a hyperbolic mirror is defined by

$$\frac{y^2}{a^2} - \frac{x^2}{b^2} = 1 \quad , a, b \in \mathbb{R} \tag{1}$$

with the semi-major axis a. The focal points $\mathcal{F}_{1,2}$ are set apart by $2\sqrt{a^2+b^2} =: 2\varepsilon$ (Fig. 3d). The robot's position is defined by the point in the middle of these two focal points. The camera's focal point coincides with $\mathcal{F}_2$. With $\vec{e}$ being the unit vector pointing from the reflection on the mirror towards the object's position $\vec{o}$:

$$\vec{e}_H(\vec{o}\,') = \frac{\left(s\vec{o}\,'_x, s\vec{o}\,'_y, \frac{a}{b}\sqrt{\rho^2+b^2} - \varepsilon\right)^\intercal}{\left|\left(s\vec{o}\,'_x, s\vec{o}\,'_y, \frac{a}{b}\sqrt{\rho^2+b^2} - \varepsilon\right)^\intercal\right|} \quad ,$$

the transformation T_H is

$$T_H : \vec{o}\,' \longmapsto \vec{o} :$$
$$\vec{o} = \vec{c} + R(\vec{q}) \left(\begin{pmatrix} so'_x \\ so'_y \\ \frac{a}{b}\sqrt{\rho(\vec{o}\,')^2 + b^2} \end{pmatrix} + d\vec{e}_H(\vec{o}\,') \right) \quad .$$

and therefore the object position at a distance d is defined as $\vec{o} = \vec{r} + R\left(\hat{\vec{o}} + \mathrm{d}\vec{e}\right)$. For the inverse transformation in polar coordinates as for the spherical shaped mirror, it can be shown radius ρ' is given by

$$\rho' = \frac{(\vec{o}-\vec{c})_\rho}{(\vec{o}-\vec{c})_\rho^2 \cdot \varepsilon^2/b^2 - 1} \left((\vec{o}-\vec{c})_z \varepsilon + a\right) \quad . \tag{2}$$

To simplify this expressions, the rotation matrix R was left out. Different camera orientations $\vec{q}$ are accounted for by rotating the vector $(\vec{o}-\vec{c})$ before calculations. The corresponding image position now found as $\vec{o}\,' = (\rho\cos\phi, \rho\sin\phi)^\intercal$.

2.2.3 Motion and Depth Estimation

Now, we can detect and track features, and, furthermore, compute the robot's displacement (translation and rotation) between consecutive frames. We keep a list of all features for all frames, which means we have the relative position of each feature from multiple positions. This enables us to perform triangulation. While in theory we would get a good estimate, real world experiments show that quite a lot of noise gets introduced.

Estimating the depth for N features adds significant complexity to the problem. Currently, we try to estimate the quadrocopter's 6D motion M—consisting of translation $\Delta\vec{r}$ and orientation $\Delta\vec{q}$. Our problem has now increased to $N + 6$ dimensions. Changes in the feature set from frame $\vec{i}_{i,t-1}$ to frame $\vec{i}_{i,t}$ provide N equations, meaning features need to be tracked for at least 3 consecutive frames.

Matching Features with the Inverse Estimation

1. Depth $d_{i,t-1}$ and motion M_t are initialized using previous data $d_{i,t-2}$ and motion M_{t-1}. The camera pose P_{t-1}, consisting of position $\vec{c}_{t-1}$ and rotation $\vec{q}_{t-1}$, is known.

2. For every feature i, calculate the global position $\vec{o}_{i,t-1}$ using the depth $d_{i,t-1}$, the image coordinates $\vec{o}\,'_{i,t-1}$ and the camera pose P_{t-1}. The transformation $T_X, X \in \{S,H\}$ is chosen according to the camera setup, as detailed above.
3. Apply the inverse motion to all global positions $\vec{o}_{i,t-1}$. This results in the predicted global positions $\vec{o}^{\,p}_{i,t}$.
4. Use the inverse transformation T_X^{-1}, to compute the predicted image position $\vec{o}\,'^{p}_{i,t} = T_X^{-1}\left(\vec{o}^{\,p}_{i,t}\right)$.
5. Lastly, we consider the environment as well as all global features to be static. Therefore, $\vec{o}_i$ and $\vec{o}\,'_i$ should be equal for corresponding features i: we minimize the sum of the squared distances for the last L time steps: $\mathrm{SD}(\mathrm{d_{i,t}}, \mathrm{M}) = \sum_{\mathrm{i=0}}^{\mathrm{N}} \sum_{\tau=-\mathrm{L}}^{0} \left\| \tilde{\mathrm{o}}'_{\mathrm{i,t}} - \tilde{\mathrm{o}}'^{,\mathrm{p}}_{\mathrm{i,t}} \right\|^2$.

Estimating the Depth with the Forward Estimation

1. Perform step 1. and 2. from the inverse estimation.
2. Our goal is to find the new depth $d_{i,t}$ based on the previous estimate $d_{i,t-1}$. In omnidirectional mirror models, the depth is $d_t = \left\| R\left(\Delta\vec{q}_t\right)\left(\vec{o} - \vec{c} - \Delta\vec{c}_t\right) - \hat{\vec{o}}^{\,p} \right\|$. The new reflection point $\hat{\vec{o}}^{\,p}$ is calculated with the inverse transformation T_X^1. For the spherical mirror, an approximation considering only rotations is easily possible. Let $\vec{k} = (0,0,b)^\intercal$ be the center of the spherical mirror. Then $\hat{\vec{o}}^{\,p} \approx R\left(\Delta\vec{q}\right)\left(\hat{\vec{o}} - \vec{k}\right) + \vec{k}$ is leading to the new depth
$$d_0 = \left\| R\left(\Delta\vec{q}_t\right)\left(\vec{o} - \vec{c} - \Delta\vec{r}_t - \hat{\vec{o}} + \vec{k}\right) - \vec{k} \right\|. \quad (3)$$
Due to $\Delta m \ll d$, the approximation can be considered to be vanishing.
3. Compute the new predicted pose $P_t = P_{t-1} + M_t$.
4. Compute predicted global positions $\vec{o}^{\,p}_{i,t=0}$ for every feature i based on the camera model.
5. The positions $\vec{o}_{i,t}$ and $\vec{o}^{\,p}_{i,t}$ should be equal for corresponding features i. We use this to minimize the sum of the squared distances
$$\mathrm{SD}(\mathrm{d_{i,t}}, \mathrm{M}) = \sum_{\mathrm{i=0}}^{\mathrm{N}} \sum_{\tau=-\mathrm{L}}^{0} \left\| \frac{\tilde{\mathrm{o}}_{\mathrm{i,t-\tau}} - \tilde{\mathrm{o}}^{\mathrm{p}}_{\mathrm{i,t-\tau}}}{\mathrm{d_{i,t-\tau}}} \right\|^2.$$
The factor $d_{i,t}$ weights all summands consistently as the position-error scales linearly with d.

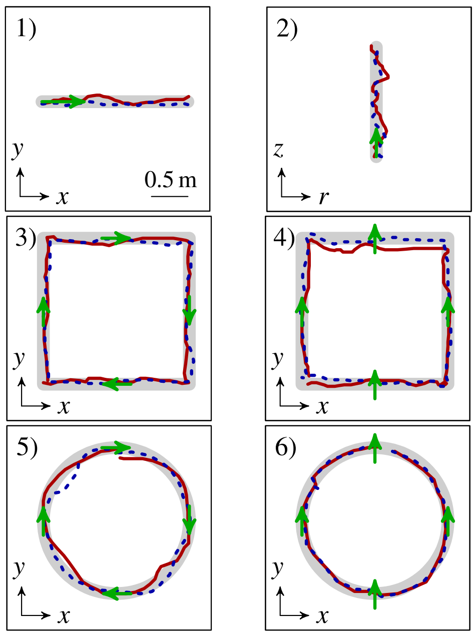

Figure 4: Qualitative examples of all target trajectory recorded while the quadrocopter was moved manually. The target trajectory is shown in gray, the quadrocopters believe state, i.e. the sensor data, in red, and external tracking results are depicted in blue. The direction of sight (this is not necessarily the direction of flight) is marked using green arrows. 1) line in $x-y$ plane; 2) lift off in z-direction plotted against the radius r; 3) square, quadrocopter pointing into direction of flight; 4) square, quadrocopter always pointing into the same direction; 5) circle, quadrocopter pointing into direction of flight; 6) circle, quadrocopter always pointing into the same direction.

2.3 Achievable Angular Resolution

Given a fixed camera resolution of $320 \times 320\,\mathrm{px}$ we can now compute the projection of the hyperbola mirror onto the camera. We assume that the object is at a distance of $2\,\mathrm{m}$ and we require five pixels width to separate it from adjacent objects. After straight forward application of above formulas, we arrive at a limit of approximately $1.9°$.

3 EXPERIMENTS

3.1 Time Performance

As we have two different setups—namely the hyperbola and the spherical mirror—we will first analyze major differences between both. Due to the shape of the spherical mirror, the area of self reflection of the robot is much larger, meaning that less features are found. We have $320 \times 320\,\mathrm{px} = 102400\,\mathrm{px}$ in total, the robot blocks 58153 px on the spherical mirror and 44892 px on the hyperbola mirror. Furthermore, we can report a 9% higher frame rate (resolution 320×320 px) for the hyperbola mirror setup due to the numerical efficiency of the explicit transformation. Full results for frame rates are shown in Table 1. Since we did not find any differences in the quality of features or flight trajectories, we focus here on the hyperbola mirror.

In Table 1 we compare our novel approach to the SVO (Forster et al., 2014) algorithm. Please note that SVO only extracts features on selected key frames and thus does not perform full computations at the reported frame rate. Also a more powerful processor was used.

3.2 Visual Odometry

We performed flights on six different target trajectories and for each path ten trials were recorded:

1. a straight line in the $x-y$ plane with length 2 m;
2. a straight line upwards into the z-direction with length 1.5 m, i.e. lift off;
3. a square with side length 2 m, the quadrocopter always pointing into the direction of flight;
4. a square with side length 2 m, the quadrocopter always pointing into the same direction;
5. a circle with diameter 2 m, the quadrocopter always pointing into the direction of flight;
6. a circle with diameter 2 m, the quadrocopter always pointing into the same direction.

An example of each trajectory is shown in Fig. 4. Each path is recorded in two different setups (this results in 120 flights total). First, the quadrocopter is moved manually on the predefined path. This allows us to quantify the visual odometry without problems that occur from flight control (e.g. rapid movements or problems with the flight control algorithms). Afterwards, we record all paths during full flight.

To achieve a meaningful evaluation, we first need to generate ground truth information: We utilize an Asus Xtion Pro camera, which offers 3D depth perception via infrared sensor. Four differently colored spherical markers are put on the quadrocopter, one on each end of the cross. This allows stable tracking of the robot's translation and rotation in indoor environments. A summary of its performance is given in (Haggag et al., 2013). We will call the Xtions data "external tracking". To give an idea of the recorded data, we have included a detailed plot of trajectory 6) during manual mode in Fig. 5.

We use the Root-Mean-Square Deviation to compute the accumulated differences in the x-y-plane (except for experiment 2, where the z and the radial component were used) as defined:

$$\mathrm{RMSD} = \sqrt{\frac{\sum_{t=1}^{n}(\vec{\hat{s}}_t - \vec{s}_t)^2}{n}}. \tag{4}$$

All results are shown in Table 2 with a graphical representation given in Fig. 6.

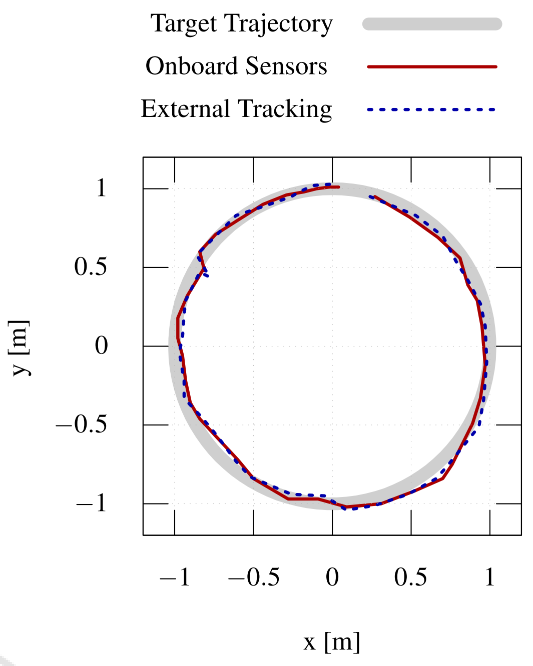

(a) The recording in the real world state space.

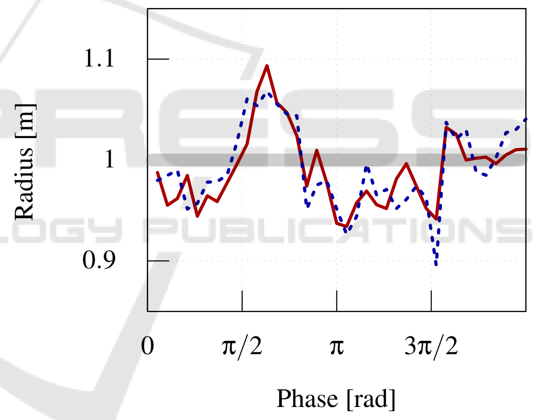

(b) Transforming the trajectory to polar coordinates shows the deviations between external tracking and onboard sensors in more detail.

Figure 5: The shown trajectory was recorded during one of the ten flights of trajectory 6) in manual mode as depicted in Fig. 4: A circle with diameter 2 m (depicted in grey), the quadrocopter always pointing into the same direction. The red line shows results from the EKF, which combines VO and IMU data. Blue dots visualize the trajectory as recorded by the external tracking system.

Table 1: Frame rates of visual odometry algorithm at different resolutions for the spherical and hyperbola mirror setup. At small resolutions only few features are found, meaning that there is only a small difference in the transformations. As more features are found at higher resolutions, the explicit transformation of the hyperbola mirror is about 9% faster (at 320 × 320 px). We compare against the SVO algorithms results as shown in (Forster et al., 2014). However, a more powerful hardware platform containing a quadcore processor with 1.6 GHz was used.

Mirror	160 × 160 px [Hz]	320 × 320 px [Hz]	640 × 640 px [Hz]
Spherical	29.8 ± 0.1	24.4 ± 0.1	15.8 ± 0.1
Hyperbola	29.7 ± 0.1	26.6 ± 0.1	17.3 ± 0.1
SVO	55 ± 1 (752 × 480 px)		

Table 2: For each of the six trajectories (as shown in Fig. 4) ten trials were performed. The averaged Root-Mean-Square Deviation in the x-y-plane for these trials is shown here. In "manual mode" the quadrocopter was moved manually on the trajectories to eliminate problems from flight control algorithms. In "Flight Mode" trials were performed in full flight mode.

Scene	Manual Mode [m]	Flight Mode [m]
1)	0.03 ± 0.01	0.07 ± 0.03
2)	0.06 ± 0.03	0.06 ± 0.03
3)	0.07 ± 0.04	0.08 ± 0.04
4)	0.05 ± 0.02	0.09 ± 0.04
5)	0.06 ± 0.03	0.11 ± 0.05
6)	0.04 ± 0.02	0.10 ± 0.04
Average	0.05 ± 0.03	0.09 ± 0.04

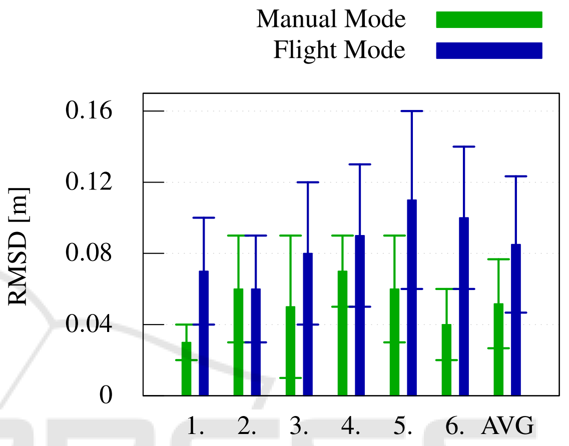

Figure 6: We compute the Root-Mean-Square Deviation in the x-y-plane between external tracking and onboard sensors. In "AVG" all six trajectories are averaged. Full results are shown in Table 2. For each scenario 10 trials were performed and values averaged.

4 DISCUSSION AND CONCLUSION

In this paper, we have investigated a novel lightweight omnidirectional camera setup for flying robots and tested it on a quadrocopter. The visual odometry is combined with IMU data and the resulting pose information is confirmed using an external tracking camera. The achieved frame rate of 26.6 ± 0.1 Hz, as shown in Table 1, is sufficient for real-time application in autonomous agents with low-power hardware. Furthermore, the deviation between external tracking and internal believe state was found to be 5 ± 3 cm in manual mode on average; in real flight self localization performs at 9 ± 4 cm. The deviation was determined in the horizontal plane for experiments 1 and 3-6 and using the z and radial coordinates for experiment 2. The utilized external tracking system performs already with an error of at least ± 1 cm (Haggag et al., 2013) and thus introducing significant uncertainty. Enhance tracking quality currently remains future work.

While the AAV's accuracy will be subject to further improvement, it is below the trajectory error of the flight controller and can therefore be used as a feedback error signal to increase trajectory control precision. Thus, we have achieved our goal to enable autonomous flight in indoor or outdoor GPS-denied areas with visual odometry.

Lastly, we will look at a real world example to give an understanding of the error margins. For this, we will assume a self localization error of 0.1 m and a frame rate of 25 Hz. Furthermore, we will assume that the AAV needs 5 frames to detect an obstacle and initiate counter measures. Using the given frame rate of 25 Hz, the quadrocopter needs 0.2 s to detect an obstacle. Within these 0.2 s the safety error margin of 0.1 m (the above localization error) must not be met. Thus, we can survey in indoor environments with a velocity of approximately 1.8 km/h. This allows for a broad range of application, e.g. fast search and rescue in impassable terrain.

Our work enables autonomous robots to localize themselves, while allowing at the same time to build a depth map. This map offers for example obstacle avoidance or mapping capabilities. All computations are performed online on embedded hardware, meaning that the robot is able to work in unknown environments. It can support autonomously, for example, in search and rescue mission, disaster relief work, or exploration tasks.

REFERENCES

Anai, T., Sasaki, T., Osaragi, K., Yamada, M., Otomo, F., and Otani, H. (2012). Automatic exterior orientation procedure for low-cost uav photogrammetry using video image tracking technique and gps information. *Int. Arch. Photogramm. Remote Sens. Spat. Inf. Sci.*

Åström, K. J. and Hägglund, T. (2006). *Advanced PID control*. ISA-The Instrumentation, Systems and Automation Society.

Augugliaro, F., Lupashin, S., Hamer, M., Male, C., Hehn, M., Mueller, M. W., Willmann, J. S., Gramazio, F., Kohler, M., and D'Andrea, R. (2014). The flight assembled architecture installation: Cooperative construction with flying machines. *IEEE Control Systems*, 34(4):46–64.

Bay, H., Tuytelaars, T., and Van Gool, L. (2006). Surf: Speeded up robust features. In *European conference on computer vision*, pages 404–417. Springer.

Demonceaux, C., Vasseur, P., and Pegard, C. (2006). Omnidirectional vision on uav for attitude computation. In *IEEE International Conference on Robotics and Automation (ICRA)*, pages 2842–2847.

Eberli, D., Scaramuzza, D., Weiss, S., and Siegwart, R. (2011). Vision based position control for mavs using one single circular landmark. *Journal of Intelligent & Robotic Systems*, 61(1–4):495–512.

El-gayar, M., Soliman, H., and Meky, N. (2013). A comparative study of image low level feature extraction algorithms. *Egyptian Informatics Journal*, 14(2):175–181.

Engel, J., Sturm, J., and Cremers, D. (2014). Scale-aware navigation of a low-cost quadrocopter with a monocular camera. *Robotics and Autonomous Systems (RAS)*, 62(11):1646–1656.

Forster, C., Pizzoli, M., and Scaramuzza, D. (2014). Svo: Fast semi-direct monocular visual odometry. In *IEEE International Conference on Robotics and Automation (ICRA)*, pages 15–22.

Gaspar, J., Grossmann, E., and Santos-Victor, J. (2001). Interactive reconstruction from an omnidirectional image. In *9th International Symposium on Intelligent Robotic Systems (SIRS01)*. Citeseer.

Haggag, H., Hossny, M., Filippidis, D., Creighton, D., Nahavandi, S., and Puri, V. (2013). Measuring depth accuracy in rgbd cameras. In *7th International Conference on Signal Processing and Communication Systems (ICSPCS)*, pages 1–7.

Heinly, J., Dunn, E., and Frahm, J.-M. (2012). Comparative evaluation of binary features. In Fitzgibbon, A., Lazebnik, S., Perona, P., Sato, Y., and Schmid, C., editors, *12th European Conference on Computer Vision (ECCV)*, pages 759–773, Berlin. Springer.

Kalman, R. E. (1960). A new approach to linear filtering and prediction problems. *Journal of basic Engineering*, 82(1):35–45.

Lange, S., Sünderhauf, N., Neubert, P., Drews, S., and Protzel, P. (2012). Autonomous corridor flight of a uav using a low-cost and light-weight rgb-d camera. In Rückert, U., Joaquin, S., and Felix, W., editors, *Advances in Autonomous Mini Robots: Proceedings of the 6-th AMiRE Symposium*, pages 183–192, Berlin. Springer.

Lowe, D. G. (1999). Object recognition from local scale-invariant features. In *The proceedings of the seventh IEEE international conference on Computer vision*, volume 2, pages 1150–1157. IEEE.

Mori, T. and Scherer, S. (2013). First results in detecting and avoiding frontal obstacles from a monocular camera for micro unmanned aerial vehicles. In *IEEE International Conference on Robotics and Automation (ICRA)*, pages 1750–1757.

Olivares-Méndez, M. A., Mondragón, I. F., Campoy, P., and Martínez, C. (2010). Fuzzy controller for uav-landing task using 3d-position visual estimation. In *Fuzzy Systems (FUZZ), 2010 IEEE International Conference on*, pages 1–8.

Quigley, M., Conley, K., Gerkey, B. P., Faust, J., Foote, T., Leibs, J., Wheeler, R., and Ng, A. Y. (2009). Ros: an open-source robot operating system. In *ICRA Workshop on Open Source Software*.

Remes, B., Hensen, D., Van Tienen, F., De Wagter, C., Van der Horst, E., and De Croon, G. (2013). Paparazzi: how to make a swarm of parrot ar drones fly autonomously based on gps. In *IMAV 2013: Proceedings of the International Micro Air Vehicle Conference and Flight Competition, Toulouse, France, 17-20 September 2013*.

Rodríguez-Canosa, G. R., Thomas, S., del Cerro, J., Barrientos, A., and MacDonald, B. (2012). A real-time method to detect and track moving objects (datmo) from unmanned aerial vehicles (uavs) using a single camera. *Remote Sensing*, 4(4):1090–1111.

Rosten, E. and Drummond, T. (2006). Machine learning for high-speed corner detection. In Leonardis, A., Bischof, H., and Pinz, A., editors, *9th European Conference on Computer Vision (ECCV)*, pages 430–443, Berlin, Heidelberg. Springer Berlin Heidelberg.

Rublee, E., Rabaud, V., Konolige, K., and Bradski, G. (2011). Orb: An efficient alternative to sift or surf. In *International conference on computer vision*, pages 2564–2571. IEEE.

Schöllig, A., Augugliaro, F., and D'Andrea, R. (2012). A platform for dance performances with multiple quadrocopters. *Improving Tracking Performance by Learning from Past Data*, page 147.

Shi, J. and Tomasi, C. (1994). Good features to track. In *IEEE Computer Society Conference on Computer Vision and Pattern Recognition*, pages 593–600. IEEE.

Teuliére, C., Eck, L., Marchand, E., and Guénard, N. (2010). 3d model-based tracking for uav position control. In *IEEE/RSJ International Conference on Intelligent Robots and Systems (IROS)*, pages 1084–1089.

Thrun, S., Montemerlo, M., Dahlkamp, H., Stavens, D., Aron, A., Diebel, J., Fong, P., Gale, J., Halpenny, M., Hoffmann, G., Lau, K., Oakley, C., Palatucci, M., Pratt, V., Stang, P., Strohband, S., Dupont, C., Jendrossek, L.-E., Koelen, C., Markey, C., Rummel, C., van Niekerk, J., Jensen, E., Alessandrini, P., Bradski, G., Davies, B., Ettinger, S., Kaehler, A., Nefian, A., and Mahoney, P. (2006). Stanley: The robot that won the DARPA grand challenge. *Journal of Field Robotics*, 23(9):661–692.

Williams, B., Cummins, M., Neira, J., Newman, P., Reid, I., and Tardós, J. (2009). A comparison of loop closing techniques in monocular SLAM. *Robotics and Autonomous Systems*, 57(12):1188–1197. Inside Data Association.